Peer-reviewed version available at *Energies* **2018**, *11*, 3000; doi:10.3390/en11113000

Article

Slope Compensation Design for a Peak Current-Mode Controlled Boost-Flyback Converter

Juan-Guillermo Muñoz[1], Guillermo Gallo[2], Fabiola Angulo[1]*, and Gustavo Osorio[1]

[1] Universidad Nacional de Colombia - Sede Manizales, Facultad de Ingeniería y Arquitectura, Departamento de Ingeniería Eléctrica, Electrónica y Computación, Percepción y Control Inteligente - Bloque Q, Campus La Nubia, Manizales, 170003 - Colombia, e-mail: {jgmunozc, fangulog, gaosoriol}@unal.edu.co

[2] Instituto Tecnológico Metropolitano, Departamento de Ingeniería Electrónica y Telecomunicaciones, Automática, Electrónica y Ciencias Computacionales (AE&CC) Group COL0053581, Medellín - Colombia, e-mail: ggalloh@unal.edu.co

* Correspondence: fangulog@unal.edu.co

Version September 27, 2018 submitted to Energies

Abstract: Power converters with coupled inductors are very promising due to the high efficiency and high voltage gain. Apart from the aforementioned advantages, the boost-flyback converter reduces the voltage stress on the semiconductors. However, to obtain good performance with high voltage gains, the controller must include two control loops (current and voltage), and a compensation ramp. One of the most used control techniques for power converters is the peak current-mode control with compensation ramp. However, in the case of a boost-flyback converter there is no mathematical expression in the literature, to compute the slope of the compensation ramp. In this paper, a formula to compute the slope of the compensation ramp is proposed in such a way that a stable period-1 orbit is obtained. This formula is based on the values of the circuit parameters, such as inductances, capacitances, input voltage, switching frequency and includes some assumptions related to internal resistances, output voltages, and some other electrical properties related with the physical construction of the circuit. The formula is verified numerically using the saltation matrix and experimentally using a test circuit.

Keywords: Slope Compensation; Coupled Inductors; Current Mode Control; Boost-Flyback Converter

1. Introduction

High step-up power converters are one of the main devices used in photovoltaic applications [1–5]. In such applications efficiency is vital, and for this reason, single-stage converters are preferable [3,4]. One way to get high gains with a single-stage of conversion is by using coupled inductors, where basics structures as boost and flyback can be coupled, improving advantages of every configurartion to extend the voltage conversion ratio, to suppress the switch voltage spike, recycle the leakage energy and get high efficiency [3,4,6]. For example, in [3], by means of coupling, a buck-boost-flyback converter is proposed. This converter consists of one MOSFET, four diodes, three inductors and three capacitors, which would suppose a high complexity in the stages of modeling and design of the controller. This due to the high order of the equations that would be generated (sixth order) and the number of semiconductors (five). In [4], a sepic-boost-flyback converter is proposed. This converter is composed by four semiconductors and eight energy storage elements, which difficulties the analysis, and also reports lower efficiencies than the converter studied in [3]. In [2,7], it is proposed the coupling of one or several cells of flyback converters with switched capacitors. Although these applications considerably increase the voltages, the complexity of the model is high, due to the great number of

Peer-reviewed version available at *Energies* **2018**, *11*, 3000; doi:10.3390/en11113000

semiconductors and energy storage elements. A good trade-off between voltage elevation, efficiency and complexity was achieved in [8,9], where by means of coupling, a boost and a flyback converter are integrated becoming a boost-flyback converter.

Since its appearance, the boost-flyback converter has been progressively improved: in [10], it is shown that the best efficiency is achieved when the turns ratio between the coupled coils is equal to two. In [11,12], it was shown that efficiency and voltage gain can be improved adding other primary and secondary coils. In [13], efficiency of the converter is improved for gains greater than eight by adding a switched coupled inductor. A drawback is that all the improvements that involve the addition of new energy storage elements or diodes increase the complexity of the system.

Due to the high voltage gain, high efficiency and low complexity, the boost-flyback converter is widely used in hybrid electric vehicles [14,15], in voltage balancing of differential power processing systems [16], in low scale arrays of photo-voltaic panels [17], in LED lighting [18,19] and in some applications of power factor correction [19]. However, the modelling, simulation and control is more difficult to do than other converters, because it has three switching devices (two diodes and one MOSFET). Nevertheless, the boost-flyback converter can be modeled as a piecewise linear dynamical system (PWLDS). A lot of work in PWLDS analysis has been reported in literature, which includes applications in power converters [20–22]. In [23], the boost-flyback converter has been modeled and analyzed using PWLDS. In that work, sliding control is applied by means of complementary model. In [24], a complete analysis of the stability and transition to chaos of this converter has been reported. in [25], the coexistence of period-1, period-2, and chaotic orbits is shown using bifurcation analysis of the coupling coefficient of the inductors.

One of the most popular control technique in power converters is the so-called peak current-mode control [26]. However, when this controller is used, it is necessary to design a compensation ramp to avoid the phenomena of fast-scale related to the inner control loop [27,28] and slow-scale due to the outer control loop [29,30]. Both dynamic behaviors have widely been studied, obtaining stability limits for period-1 orbits, in [31,32], using a frequency analysis are included the output voltage ripple effects to find a more precise expression for compensation ramp. On the other hand, in [33,34], a steady-state approach is used to obtain stability limits. However, in these works only two switching configurations has been taken into account, when in practice the boost-flyback converter presents four switching configurations making difficult to calculate a precise mathematical expression for the slope of the compensation ramp to avoid subharmonics.

In this paper, an analytical expression to determine the value of the slope compensation for a boost-flyback converter with peak current-mode control is calculated, which includes only fast-scale phenomenons. Computations are made assuming ideal circuit elements and the results are compared with numerical simulations obtained using models with internal resistors as well as with experiments. For numerical comparisons, bifurcation diagrams and the Largest Absolute Value of the Eigenvalues (LAVE) are computed. The bifurcation diagram are computed by brute force, and the LAVEs use the solutions of the dynamical equations which are determined by the monodromy matrix and the saltation matrix for the switching instants [35]. The experiments are carried out in a lab prototype of 100 Watts. All results show good agreement and small deviations are presumably due to the fact that internal resistances are not considered in the simplified model.

The rest of the paper is organized as follows. In section II, the operation mode of the boost-flyback converter is explained, as well as the peak-current mode control. In section III, the computations to obtain the mathematical expression for the slope compensation are presented. In section IV, numerical results are shown and compared. These are obtained using the derived formula for a particular example of the converter using parameters similar to those in the experimental set up including the non-ideal model (internal resistance for some of the components). In section V, the experimental results attained with a 100 Watts lab prototype are presented and compared with the results in previous sections. Finally, in Section VI the conclusions are given.

Preprints (www.preprints.org) | NOT PEER-REVIEWED | Posted: 28 September 2018 doi:10.20944/preprints201809.0554.v1

Peer-reviewed version available at Energies 2018, 11, 3000; doi:10.3390/en11113000

2. Mathematical Modeling

2.1. Boost-Flyback Converter

A boost-flyback power converter is depicted in figure 1. It mainly consists of two coupled inductors (L_p, L_s), two capacitors (C_1, C_2), one MOSFET (S), and two diodes (D_1, D_2). The MOSFET is controlled while the diodes commutate depending on their polarization. As the name states, it is the union of a boost and a flyback converter, and it allows to obtain high gain and high efficiency while the stress voltage in the semiconductor devices decreases in comparison with a standard flyback [9,10].

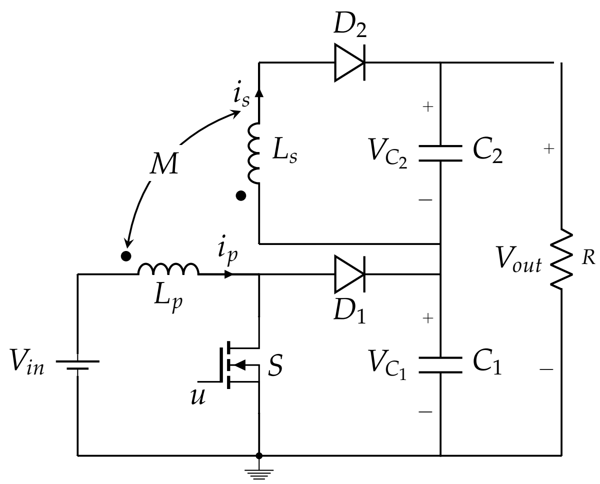

Figure 1. Boost-flyback converter topology.

As the semiconductor devices are three, there are eight possible switch configurations or states: E_1... E_8. However, it has been shown that only six states have physical meaning [23] and in [24] it was proven that the controlled system exhibits a period-1 orbit switching among four states such as is described in Table 1. A schematic diagram of the steady state current behavior in a period-1 solution is presented in figure 2. The states E_1 and E_2 are present when the MOSFET is on, and the states E_3 and E_4 are present when the MOSFET is off.

Table 1. States of the period-1 orbit

State	S	D_2	D_1
E_1	ON	ON	OFF
E_2	ON	OFF	OFF
E_3	OFF	ON	ON
E_4	OFF	ON	OFF

Starting from E_1 the system evolves as follows: $E_1 \mapsto E_2 \mapsto E_3 \mapsto E_4$. The change from E_1 to E_2 is given when $i_s = 0$ at $t = t_1$; the system changes from E_2 to E_3 when the switching condition is satisfied at $t = DT$, which is called the duty cycle and corresponds to the ratio between the time the MOSFET is on and the period T, *i.e*: $D = t_{u=1}/T$; E_3 changes to E_4 when $i_p = 0$ at $t = t_2$ and finally at $t = T$ the system returns to E_1. The set of differential equations describing the period-1 orbit are:

Peer-reviewed version available at Energies 2018, 11, 3000; doi:10.3390/en11113000

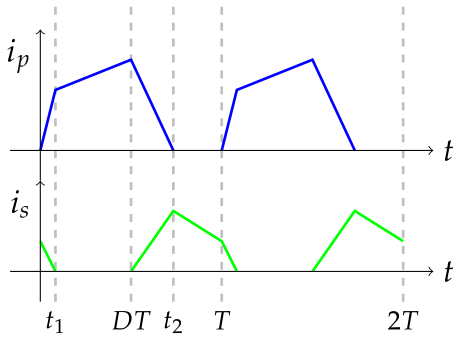

Figure 2. Typical behavior of the currents flowing by the coils in steady state of a period-1 orbit.

99 • State 1: E_1, $t \in [kT \;\; kT + t_1]$:

$$\begin{aligned}
\frac{di_p}{dt} &= \frac{(L_s V_{in} + M V_{C_2})}{n} \\
\frac{di_s}{dt} &= \frac{(-M V_{in} - L_p V_{C_2})}{n} \\
\frac{dV_{C_1}}{dt} &= -\frac{(V_{C_1} + V_{C_2})}{RC_1} \\
\frac{dV_{C_2}}{dt} &= \frac{i_s}{C_2} - \frac{(V_{C_1} + V_{C_2})}{RC_2}
\end{aligned} \tag{1}$$

100 • State 2: E_2, $t \in (kT + t_1 \;\; kT + DT]$:

$$\begin{aligned}
\frac{di_p}{dt} &= \frac{V_{in}}{L_p} \\
\frac{di_s}{dt} &= 0 \\
\frac{dV_{C_1}}{dt} &= -\frac{(V_{C_1} + V_{C_2})}{RC_1} \\
\frac{dV_{C_2}}{dt} &= -\frac{(V_{C_1} + V_{C_2})}{RC_2}
\end{aligned} \tag{2}$$

101 • State 3: E_3, $t \in (kT + DT \;\; kT + t_2]$:

$$\begin{aligned}
\frac{di_p}{dt} &= \frac{(L_s (V_{in} - V_{C_1}) + M V_{C_2})}{n} \\
\frac{di_s}{dt} &= \frac{(-M (V_{in} - V_{C_1}) - L_p V_{C_2})}{n} \\
\frac{dV_{C_1}}{dt} &= \frac{i_p}{C_1} - \frac{(V_{C_1} + V_{C_2})}{RC_1} \\
\frac{dV_{C_2}}{dt} &= \frac{i_s}{C_2} - \frac{(V_{C_1} + V_{C_2})}{RC_2}
\end{aligned} \tag{3}$$

Preprints (www.preprints.org) | NOT PEER-REVIEWED | Posted: 28 September 2018 doi:10.20944/preprints201809.0554.v1

Peer-reviewed version available at Energies 2018, 11, 3000; doi:10.3390/en11113000

- State 4: E_4, $t \in (kT + t_2 \;\; kT + T)$:

$$
\begin{aligned}
\frac{di_p}{dt} &= 0 \\
\frac{di_s}{dt} &= -\frac{V_{C_2}}{L_s} \\
\frac{dV_{C_1}}{dt} &= -\frac{(V_{C_1} + V_{C_2})}{RC_1} \\
\frac{dV_{C_2}}{dt} &= \frac{i_s}{C_2} - \frac{(V_{C_1} + V_{C_2})}{RC_2}
\end{aligned} \tag{4}
$$

Where V_{in} is the input voltage, i_p and i_s are the primary and secondary currents, V_{C_1} and V_{C_2} are the voltages across the capacitors C_1 and C_2, $M = k\sqrt{L_p L_s}$ is the mutual inductance which depends on the coupling coefficient k and $n = L_p L_s - M^2$. The output voltage is $V_{out} = V_{C_1} + V_{C_2}$.

The peak current-mode control is a widely used technique for the control of power converters [24,27,31]. A general schematic diagram of the boost-flyback converter with the proposed controller is depicted in figure 3. When a peak current-mode control is used, a fixed switching frequency is obtained and the behavior of the currents are very similar to those depicted in figure 2. At the beginning of the period the MOSFET is active, the current i_p grows and the current i_s decreases down to $i_s = 0$; at this time instant (t_1) the dynamical equations describing the system change but the MOSFET continues on until i_p is equal to the reference current I_c^* just at $t = DT$. At $t = DT$ the switches turns off until the next cycle starts again. The signal I_c^* is composed by two parts: the first one (noted as I_c) is provided by a PI controller applied to the output voltage error $e = V_{ref} - V_{out}$. The second one corresponds to the signal supplied by the compensation ramp $V_r = \frac{A_r}{T}\mathrm{mod}(t/T)$. In this way, the reference current can be expressed as:

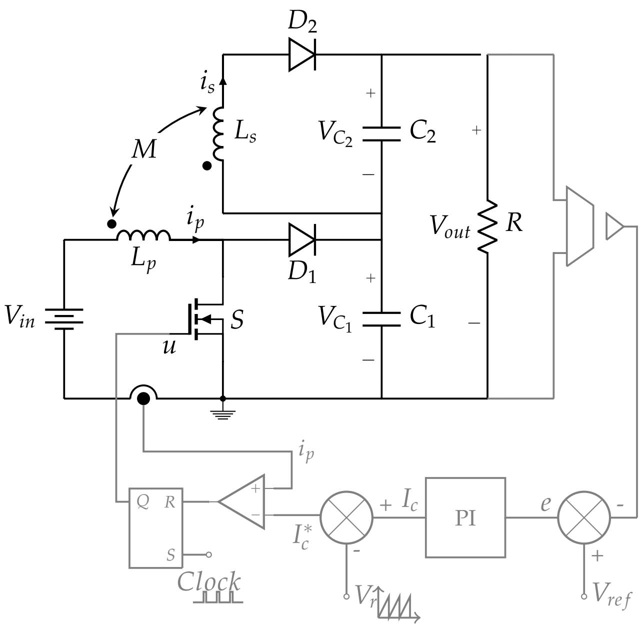

Figure 3. Boost-flyback converter with peak current-mode control.

$$
I_c^* = k_p e + k_i \int e\,dt - \frac{A_r}{T}\mathrm{mod}(t/T) \tag{5}
$$

(6)

Preprints (www.preprints.org) | NOT PEER-REVIEWED | Posted: 28 September 2018 doi:10.20944/preprints201809.0554.v1

Peer-reviewed version available at Energies 2018, 11, 3000; doi:10.3390/en11113000

where k_p and k_i are the parameters associated to the PI controller and A_r corresponds to the amplitude of the compensation ramp. Thanks to the flip-flop, there is only one switching cycle per period. At the beginning of the period the switch turns on and it remains on until the switching condition $i_p = I_c$ is achieved (just the corresponding duty cycle). When $i_p = I_c$ the switch opens and it holds opens until the next period starts. Taking into account sliding is not possible (*i.e.* there is only one commutation per cycle), the switching condition can be expressed as:

$$U = \begin{cases} 1 & \text{if } 0 \leq t < DT, \\ 0 & \text{if } DT \leq t < T. \end{cases} \tag{7}$$

Where $D \in [0, 1]$ is the duty cycle.

3. Slope Compensation Design

As far as the authors know, it has not been reported in the specialized literature a procedure to determine the slope of the compensation ramp for a boost-flyback converter, such that can be used to attain stability of the period-1 orbit. The objective of this section is to analyze the slopes of the currents flowing through the inductors in order to find an analytical expression to determine the slope of the compensation ramp, such that guarantees the stability of the period-1 orbit. In figure 4, represents the behavior of the currents flowing through primary and secondary coils when the system works in the period-1 orbit described by states E_1, E_2, E_3 and E_4, and the slopes are clearly marked in the figure.

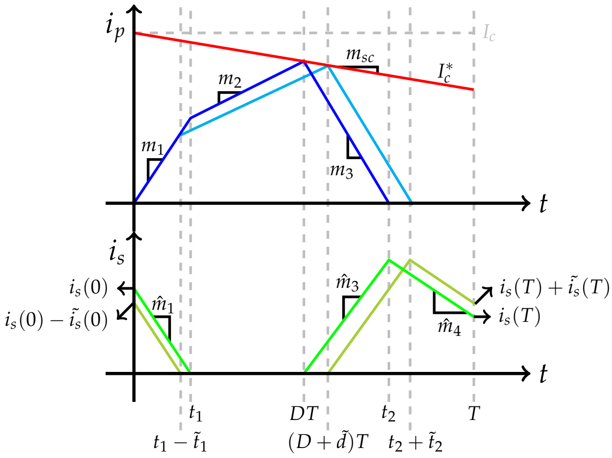

Figure 4. Primary- and secondary-coil currents for the period-1 orbit and a perturbed solution.

3.1. Assumptions

In the analysis, the following approximations are considered: *i)* for all elements and devices the internal resistances are zero. *ii)* the steady state output of the PI-controller (I_c) is constant and hence its derivative is zero; however, as it can be seen in the procedure, the constant value is not needed to compute the final expression. *iii)* the voltages V_{C_1} and V_{C_2} are constant and they can be computed as a

Preprints (www.preprints.org) | NOT PEER-REVIEWED | Posted: 28 September 2018 doi:10.20944/preprints201809.0554.v1

Peer-reviewed version available at Energies 2018, 11, 3000; doi:10.3390/en11113000

function of the duty cycle D. V_{C_1} is just the output of the boost part, V_{C_2} is the output of the flyback part, taking into account the coupling factor is lower than $k \lesssim 1$.

$$\begin{aligned} V_{C_1} &= \frac{1}{(1-D)} V_{in} \\ V_{C_2} &= \frac{(1-\frac{M}{Lp})}{(\frac{M}{L_s}-1)} \frac{D}{(1-D)} V_{in} \\ V_{out} &= \frac{1+\frac{(1-\frac{M}{Lp})}{(\frac{M}{L_s}-1)} D}{1-D} V_{in}. \end{aligned} \tag{8}$$

and *iv)* all currents can be expressed mathematically like straight lines, such that the slopes associated to i_p are m_1, m_2 and m_3, and the slopes associated to i_s are $\hat{m}_1$, $\hat{m}_3$ and $\hat{m}_4$ (see figure 4). These slopes can be computed from equations (1), (2), (3) and (4), as follows:

$$\begin{aligned} m_1 &= \frac{L_s V_{in} + M V_{C_2}}{n} \\ \hat{m}_1 &= \frac{-M V_{in} - L_p V_{C_2}}{n} \\ m_2 &= \frac{V_{in}}{L_p} \\ m_3 &= \frac{L_s(V_{in} - V_{C_1}) + M V_{C_2}}{n} \\ \hat{m}_3 &= \frac{-M(V_{in} - V_{C_1}) - L_p V_{C_2}}{n} \\ \hat{m}_4 &= -\frac{V_{C_2}}{L_s} \end{aligned} \tag{9}$$

In a similar way as the slope compensation in a boost power converter is designed considering the stability of the period-1 orbit [26], in this paper we propose an analysis of the stability of the period-1 orbit using the information of the current slopes and the conditions that should be fulfilled to guarantee the stability of the controlled system. To analyze the stability of the period-1 orbit a small perturbation is added at the beginning of the cycle and its corresponding value at the end of the period T is computed. If the magnitude of the perturbation increases, then the period-1 orbit is unstable; on the contrary, if the magnitude of the perturbation decreases, then the orbit is stable.

3.2. Mathematical Procedure

Analysis of current in the primary coil

At the swiching time $t = DT$ a pair of equations are fulfilled: One of them to its left and the other one to its rigth. Defining the slope of the compensation ramp as $m_{sc} = \frac{Ar}{T}$, it can be seen that just at the switching time the following equation is satisfied:

$$I_c - m_{sc} DT = m_1 t_1 + m_2 (DT - t_1) \tag{10}$$

Considering a perturbation in the initial condition, the last equation can be expressed as:

$$I_c - m_{sc}(D + \tilde{d})T = m_1(t_1 - \tilde{t}_1) + m_2((D + \tilde{d})T - (t_1 - \tilde{t}_1)) \tag{11}$$

Subtracting equation (11) from (10), we obtain:

$$m_{sc}\tilde{d}T = m_1\tilde{t_1} - m_2(\tilde{d}T + \tilde{t_1}) \tag{12}$$

From (12)

$$\tilde{t_1} = \frac{(m_{sc} + m_2)}{(m_1 - m_2)}\tilde{d}T \tag{13}$$

In a similar way, the analysis at the right of the switching time leads to the next equation.

$$I_c - m_{sc}DT - m_3(t_2 - DT) = 0 \tag{14}$$

Taking into account the perturbation, this equation is given by:

$$I_c - m_{sc}(D + \tilde{d})T - m_3((t_2 + \tilde{t}_2) - (D + \tilde{d})T) = 0 \tag{15}$$

Subtracting (15) from (14)

$$m_{sc}\tilde{d}T + m_3(\tilde{t}_2 - \tilde{d}T) = 0 \tag{16}$$

From (16),

$$\tilde{t_2} = \frac{(m_3 - m_{sc})}{m_3}\tilde{d}T \tag{17}$$

152

153 **Analysis of current in the secondary coil**

Now, the expressions for the current i_s and its perturbation $\tilde{i}_s(0)$ are computed. At $t = t_1$ they are:

$$i_s(0) - \hat{m}_1 t_1 = 0 \tag{18}$$

and

$$i_s(0) - \tilde{i}_s(0) - \hat{m}_1(t_1 - \tilde{t}_1) = 0 \tag{19}$$

Subtracting (19) from (18), it is obtained

$$\tilde{i}_s(0) = \hat{m}_1\tilde{t}_1 \tag{20}$$

Replacing (13) in (20), we have:

$$\tilde{i}_s(0) = \hat{m}_1\frac{(m_{sc} + m_2)}{(m_1 - m_2)}\tilde{d}T \tag{21}$$

From this equation $\tilde{d}T$ can be expressed as:

$$\tilde{d}T = \frac{\tilde{i}_s(0)}{\hat{m}_1\frac{(m_{sc}+m_2)}{(m_1-m_2)}} \tag{22}$$

Now, at $t = t_2$ the following equation is fulfilled,

$$\hat{m}_3(t_2 - DT) - \hat{m}_4(T - t_2) = i_s(T) \tag{23}$$

At the same time $t = t_2$, the perturbed equation is:

$$\hat{m}_3((t_2 + \tilde{t}_2) - (D + \tilde{d})T) - \hat{m}_4(T - (t_2 + \tilde{t}_2)) = i_s(T) + \tilde{i}_s(T) \tag{24}$$

Preprints (www.preprints.org) | NOT PEER-REVIEWED | Posted: 28 September 2018 doi:10.20944/preprints201809.0554.v1

Peer-reviewed version available at Energies 2018, 11, 3000; doi:10.3390/en11113000

Now, subtracting (23) from (24), we have:

$$\tilde{i}_s(T) = (\hat{m}_3 + \hat{m}_4)\tilde{t}_2 - \hat{m}_3 \tilde{d}T \tag{25}$$

Replacing (17) en (25), we obtain:

$$\tilde{i}_s(T) = \left(\hat{m}_4 - m_{sc}\frac{(\hat{m}_3 + \hat{m}_4)}{m_3} \right) \tilde{d}T \tag{26}$$

Finally, replacing equation (22) in (26) we find an expression that relates the secondary coil current at the beginning of the cycle, with its value at the end of it. This expression is given by:

$$\tilde{i}_s(T) = \alpha \tilde{i}_s(0) \tag{27}$$

where

$$\alpha = \left[\frac{(\hat{m}_4 - m_{sc}\frac{(\hat{m}_3+\hat{m}_4)}{m_3})}{\hat{m}_1 \frac{(m_{sc}+m_2)}{(m_1-m_2)}} \right] \tag{28}$$

Stability condition

Then, the stability of the period-1 orbit is given by the absolute value of α. If $|\alpha| > 1$ the periodic orbit is unstable, if $|\alpha| < 1$ it is asymptotically stable, and $|\alpha| = 1$ corresponds to the limit of the stability. To guarantee that the system operates in a period-1 orbit the slope of the compensation ramp must satisfy the following expression:

$$m_{sc} = \frac{A_r}{T} > \frac{m_3(\hat{m}_4(m_1 - m_2) - \hat{m}_1 m_2)}{\hat{m}_1 m_3 + (\hat{m}_3 + \hat{m}_4)(m_1 - m_2)} \tag{29}$$

4. Results

4.1. Numerical Results

The parameter values used for simulations and experiments are given in Table 2. The voltages V_{C_1} and V_{C_2} are computed from equation (8), the slopes of the straight lines are calculated using equation (9), the output voltage V_{out} corresponds to the desired output voltage V_{ref} and $|\alpha| = 1$. With these data, the desired output voltage is varied and the limit value of the slope compensation m_{sc} is obtained. Figure 5(a) shows the results obtained when the proposed approach is used (see (29)) and $V_{ref} \in (90, 130)$. Figure 5(b) presents the exact computation using the saltation matrix. Values of A_r grater than the stability limit guarantee stability of a period-1 orbit. In addition, for $V_{ref} = 100V$ the limit value for the compensation ramp is close to $A_r = 1.94$ and for $V_{ref} = 120V$ is close to $A_r = 3.25$ (see figure 5). Figure 6 shows the comparison between the analytical approach proposed in this paper and the exact value obtained with the saltation matrix; the result is expressed in percentage of the error. As it is shown, the lower the reference voltage, the higher error there is. In fact, for gain factors upper than six, the approach behaves better.

4.2. Experimental results

To validate the numerical results, an experimental lab prototype able to deliver 100 Watts to the load was designed and implemented as it is shown in figure 7. A complete design of the circuit is shown in rigure 8. A ferrite core type E is used to design the coupled inductors and the number of turns were calculated with the approach proposed in [36]. The values of the different elements of the circuit are given in Tables 2 and 3. The current in the primary coil is measured with a non-inductive shunt-resistance r_{shunt} (LTO050FR0100FTE3) followed by an instrumentation amplifier IC_1; the output voltage is measured through a voltage divider which consists of R_a and R_b. The signal from the voltage

doi:10.20944/preprints201809.0554.v1

Peer-reviewed version available at *Energies* **2018**, *11*, 3000; doi:10.3390/en11113000

Table 2. Parameter values of the converter

Parameters	
V_{in}	18V
L_p	129.2 μH
L_s	484.9 μH
r_p	0.0268Ω
r_{shunt}	0.01Ω
r_s	0.1307Ω
k	0.995
C_1	220μF
C_2	220μF
R	200Ω
k_p	2
k_i	350
T	$1/(20KHz)$

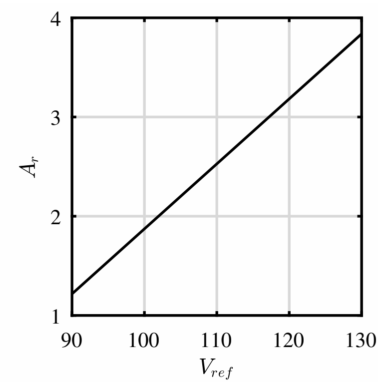

(a)

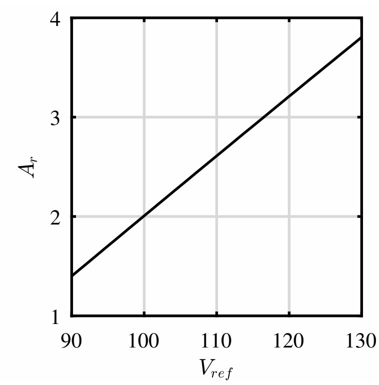

(b)

Figure 5. Value of the slope compensation. (a) Approach proposed in this paper. (b) Exact value obtained with the saltation matrix.

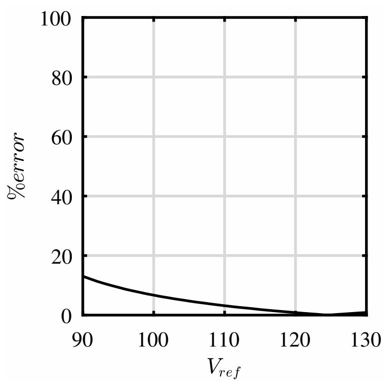

Figure 6. Percentage of error of the slope compensation.

divider feeds other amplifier IC_1. The $MOSFET$ is an $IRFP260N$ which has low internal resistance. Finally, two ultra-fast diodes $RHRP30120$ (D_1 and D_2) are used.

The controller is implemented using operational amplifiers (IC_2). The compensation ramp and the clock signals are generated using an $LM555$ (IC_4). The amplitude of the compensation ramp is adjusted with a span resistor R_{span} and V_B compensates the offset. The constants k_p and k_i are associated to the PI controller, and they are obtained from R_2, R_3, R_4 and C_3. The measured signals

Preprints (www.preprints.org) | NOT PEER-REVIEWED | Posted: 28 September 2018 doi:10.20944/preprints201809.0554.v1
Peer-reviewed version available at Energies 2018, 11, 3000; doi:10.3390/en11113000

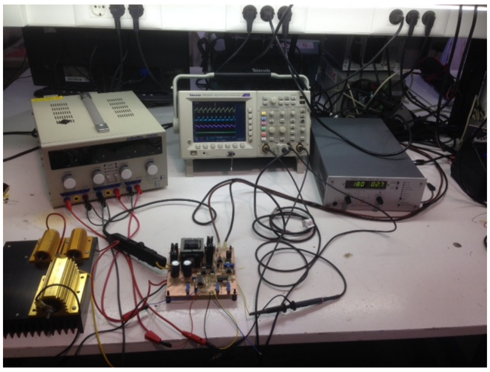

Figure 7. Experimental implementation

Table 3. Other parameter associated to the experiment.

Element	Value	Electronic Device	Reference
R_a	1MΩ	IC_1	INA128p
R_b	20kΩ	IC_2	TL084
R_1	100kΩ	IC_3	LM311
R_2	5.7kΩ	IC_4	555
R_3	10kΩ	IC_5	74XX02
R_4	200kΩ	IC_6	IRF2110
R_t	2.2kΩ	IC_7	74XX08
C_3	0.1μF	Q_T	2N3906
C_4	10nF	D	1N4148

were scaled to 0.196 using the voltage gains (A_{g_1} and A_{g_2}). The constant G_v is given by the voltage divider $R_b/(R_a + R_b)$.

Four experiments to validate the results obtained in the previous section are carried out. All figures of the experimental results show the reference current I_c^*, the current in the primary coil i_p, the current in the secondary coil i_s and the output voltage V_{out}. Therefore, the output voltage and the current in the secondary coil are scaled by a factor of 10. The reference current and the current in the primary coil are scaled by a factor of 0.196 as it was mentioned before.

For $V_{ref} = 100$V (the load resistance is fixed to $R = 200\Omega$, Table 2), two values of the slope compensation are tuned: $A_r = 1.8$ and $A_r = 2.2$. When $A_r = 1.8$ the limit set is a period-2 orbit as it shows in figure 9, but if the ramp compensation increases to $A_r = 2.2$, it changes to a period-1 orbit (figure 10).

Preprints (www.preprints.org) | NOT PEER-REVIEWED | Posted: 28 September 2018 doi:10.20944/preprints201809.0554.v1

Peer-reviewed version available at Energies 2018, 11, 3000; doi:10.3390/en11113000

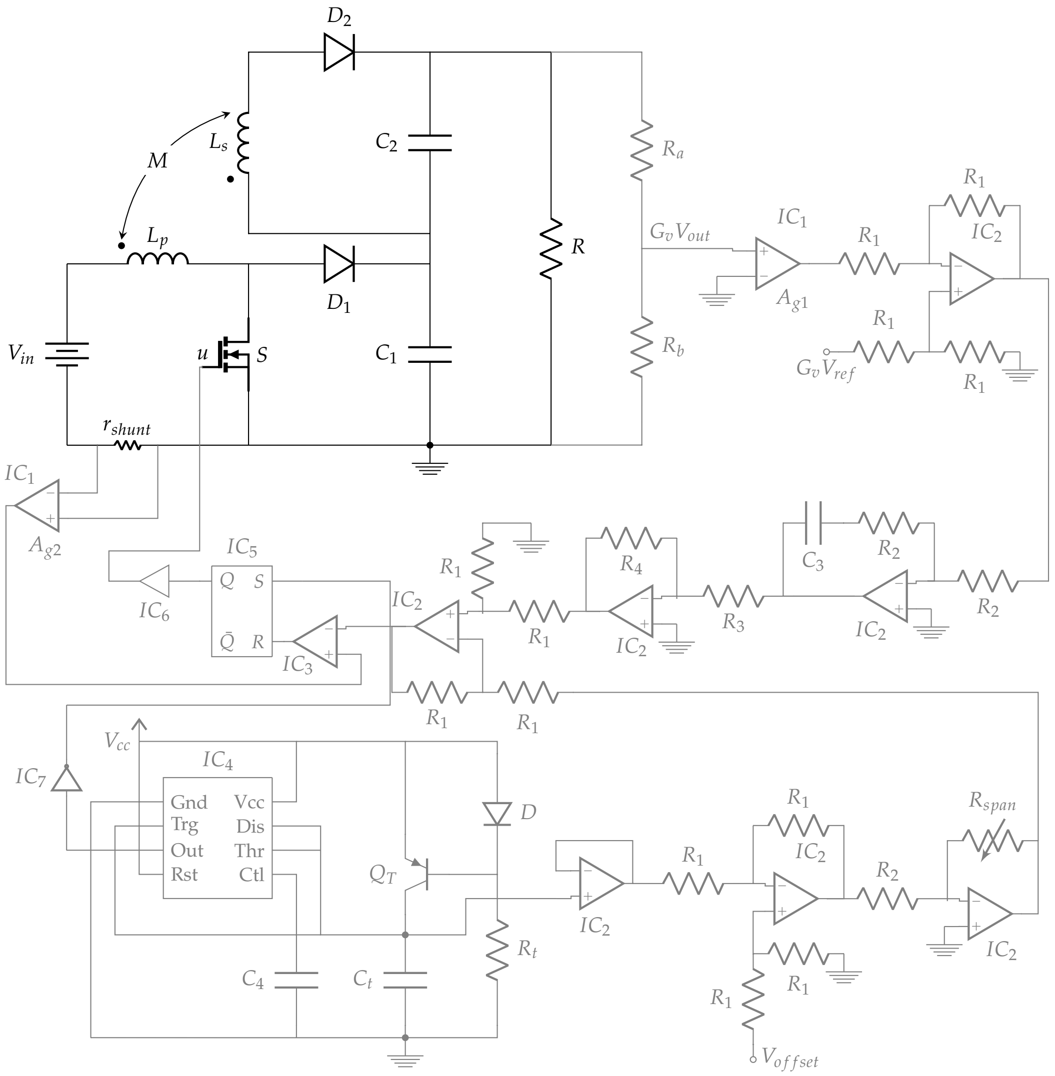

Figure 8. Experimental Circuit.

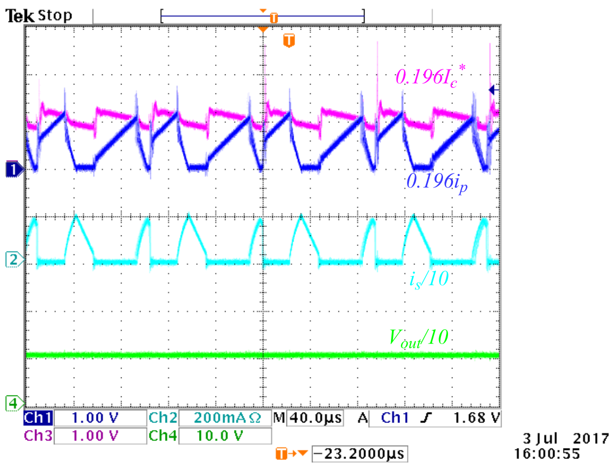

Figure 9. i_p for $V_{ref} = 100$V and $A_r = 1.8$.

Preprints (www.preprints.org) | NOT PEER-REVIEWED | Posted: 28 September 2018 doi:10.20944/preprints201809.0554.v1
Peer-reviewed version available at Energies 2018, 11, 3000; doi:10.3390/en11113000

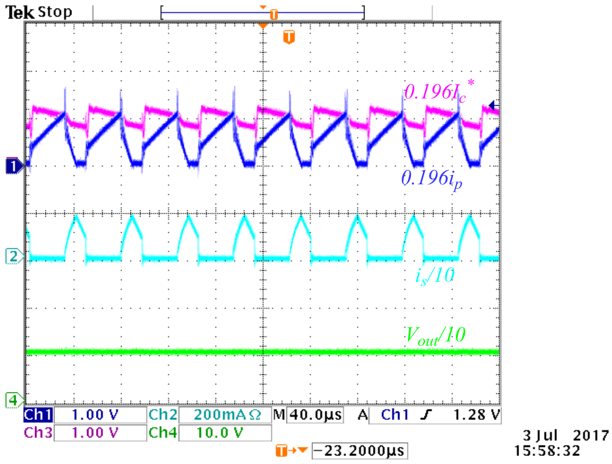

Figure 10. i_p for $V_{ref} = 100$V and $A_r = 2.2$.

In the second experiment $V_{ref} = 120V$. In a similar way, two values of the slope compensation are tuned: $A_r = 3$ and $A_r = 3.4$. The behavior of I_c^*, i_p, i_s and V_{out} are shown in figures 11 and 12. For $A_r = 3$ a high-period orbit appears, and for $A_r = 3.4$ the period-1 orbit is stable. These results agree with the information provided by equation (29), and this formula is adequate for tuning the slope of the compensation ramp.

5. Conclusions

This paper enhances the knowledge of the controller design for a boost-flyback converter which is currently a field of study.

To obtain high gains with a stable period-1 orbit when a boost-flyback converter is used, it is necessary to add a compensation ramp in the design. In this paper, an analytical expression to compute the value of the compensation ramp slope was found and mathematically proven. For gains greater than six, the approach developed in this paper has an error lower than 5%.

In a general way, the results obtained from the equation derived from our computations agree with the experiments, there is a small disagreement in comparison with the exact solution for gains lower than six, mainly because some of the assumptions are to strong for the real system, which were not included in the model for the sake of simplicity. This difference is neglectable for high step-up gains, for which our approach provides the major benefit of having a formula to guarantee stability avoiding over-compensation or very complex computations.

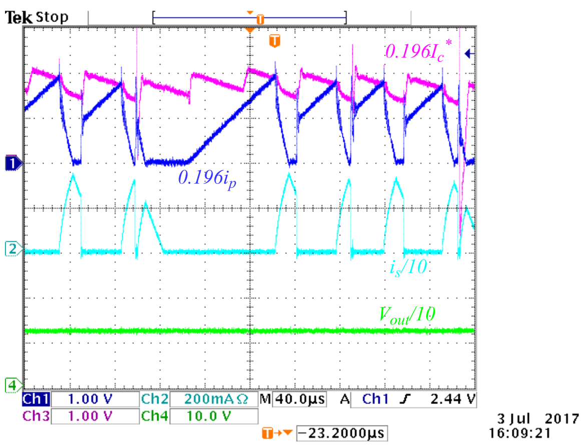

Figure 11. i_p for $V_{ref} = 120$V and $A_r = 3$

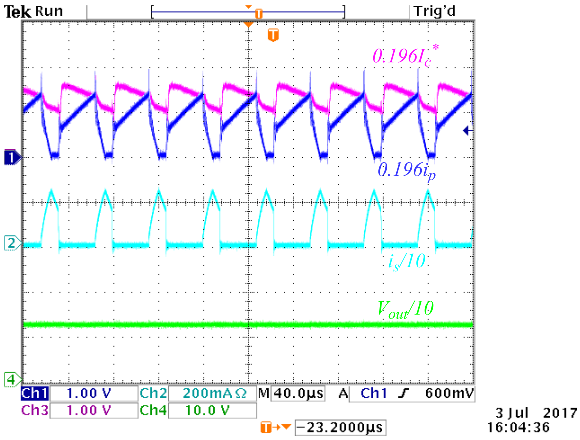

Figure 12. i_p for $V_{ref} = 120$V and $A_r = 3.4$

212 **Author Contributions:** Conceptualization, Fabiola Angulo; Formal analysis, Juan-Guillermo Muñoz and Fabiola Angulo; Funding acquisition, Fabiola Angulo and Gustavo Osorio; Investigation, Juan-Guillermo Muñoz; Project administration, Fabiola Angulo; Software, Juan-Guillermo Muñoz, Guillermo Gallo and Gustavo Osorio; Supervision, Fabiola Angulo and Gustavo Osorio; Validation, Juan-Guillermo Muñoz; Writing – original draft, Juan-Guillermo Muñoz and Guillermo Gallo; Writing – review editing, Fabiola Angulo and Gustavo Osorio.

FundingThis work was supported by Universidad Nacional de Colombia, Manizales, Project 31492 from Vicerrectoría de Investigación, DIMA, and COLCIENCIAS under Contract FP44842-052-2016 and program Doctorados Nacionales 6172-2013.

Acknowledgments: The authors would like to thank Dr. Ángel Cid Pastor and Dr. Abdelali el Aroudi from GAEI Research Center, Universitat Rovira i Virgili, SPAIN, for their assistance in getting experimental results.

Conflicts of Interest: The authors declare no conflict of interest. The founding sponsors had no role in the design of the study; in the collection, analyses, or interpretation of data; in the writing of the manuscript, and in the decision to publish the results.

Appendix A

In this appendix, the procedure to find the ratio between input and output voltages for a flyback converter when copuling factor k is different from zero is presented

$$V_{C_2} = \frac{n_2}{n_1}\frac{D}{1-D} \tag{30}$$

The flyback converter operates in two topologies named state 1 and state 2, which are depicted in figure 13. Voltage equations in primary and secodary coils are given in general form as:

$$\begin{aligned} v_{L_p} &= L_p\frac{di_p}{dt} + M\frac{di_s}{dt} \\ v_{L_s} &= L_s\frac{di_s}{dt} + M\frac{di_p}{dt}. \end{aligned} \tag{31}$$

Depending on the state, voltages and currents can be approximated as:

State 1

$$\begin{aligned} v_{L_{p}1} &\approx V_{in} \\ v_{L_{s}1} &\approx \frac{M}{L_p}V_{in} \\ i_{C1} &\approx -V_{C_2}/R \end{aligned} \tag{32}$$

State 2

Peer-reviewed version available at Energies 2018, 11, 3000; doi:10.3390/en11113000

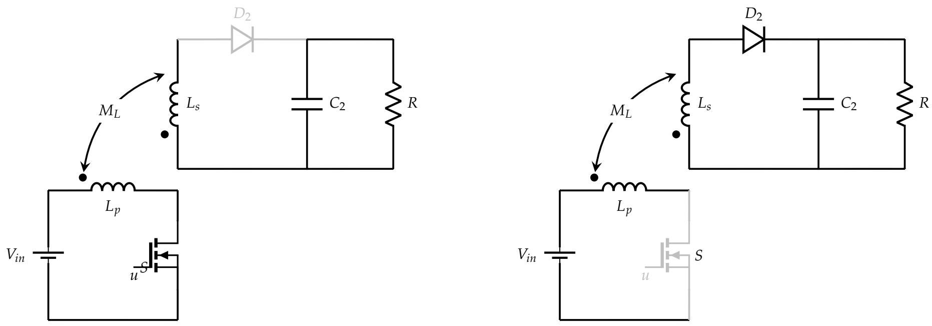

Figure 13. Flyback converter topologies.

$$\begin{aligned} v_{L_p 2} &\approx -\frac{M}{L_s} V_{C_2} \\ v_{L_s 2} &\approx -V_{C_2} \\ i_{C2} &\approx i_{L_s} - V_{C_2}/R, \end{aligned} \tag{33}$$

231 such that the average values can be calculated as:

$$\begin{aligned} < v_{L_p} > &= DV_{in} - (1-D)\frac{M}{L_s}V_{C_2} = 0 \\ < v_{L_s} > &= D\frac{M}{L_p}V_{in} - (1-D)V_{C_2} = 0 \\ < i_C > &= -DV_{C_2}/R + (1-D)(i_{L_s} - V_{C_2}/R) = 0. \end{aligned} \tag{34}$$

232 Taking into account $k < 1$, i.e. $\frac{M}{Lp} \neq \frac{Ls}{M}$, we have

$$DV_{in} - (1-D)\frac{M}{L_s}V_{C_2} = D\frac{M}{L_p}V_{in} - (1-D)V_{C_2}, \tag{35}$$

233 to finally find

$$\frac{V_{C_2}}{V_{in}} = \frac{(1-\frac{M}{Lp})}{(\frac{M}{L_s}-1)}\frac{D}{(1-D)} \tag{36}$$

234 Doing $k = 1$, it is easy to prove that this ratio is the same as the reported for a non magnetically coupled
235 flyback converter.

236

237 1. Wu, Y.E.; Chiu, P.N. A High-Efficiency Isolated-Type Three-Port Bidirectional DC/DC Converter for
238 Photovoltaic Systems. *Energies* **2017**, *10*.
239 2. Choudhury, T.R.; Dhara, S.; Nayak, B.; Santra, S.B. Modelling of a high step up DC-DC converter based on
240 Boost-flyback-switched capacitor. 2017 IEEE Calcutta Conference (CALCON), 2017, pp. 248–252.
241 3. Shen, C.L.; Chiu, P.C. Buck-boost-flyback integrated converter with single switch to achieve high voltage
242 gain for PV or fuel-cell applications. *IET Power Electronics* **2016**, *9*, 1228–1237.
243 4. Lodh, T.; Majumder, T. Highly efficient and compact Sepic-Boost-Flyback integrated converter with
244 multiple outputs. 2016 International Conference on Signal Processing, Communication, Power and
245 Embedded System (SCOPES), 2016, pp. 6–11.
246 5. Arango, E.; Ramos-Paja, C.A.; Calvente, J.; Giral, R.; Serna, S. Asymmetrical Interleaved DC/DC Switching
247 Converters for Photovoltaic and Fuel Cell Applications-Part 1: Circuit Generation, Analysis and Design.
248 *Energies* **2012**, *5*, 4590–4623.

6. Liu, H.; Hu, H.; Wu, H.; Xing, Y.; Batarseh, I. Overview of High-Step-Up Coupled-Inductor Boost Converters. *IEEE Journal of Emerging and Selected Topics in Power Electronics* **2016**, *4*, 689–704.
7. Wang, Y.F.; Yang, L.; Wang, C.S.; Li, W.; Qie, W.; Tu, S.J. High Step-Up 3-Phase Rectifier with Fly-Back Cells and Switched Capacitors for Small-Scaled Wind Generation Systems. *Energies* **2015**, *8*, 2742–2768.
8. Zhao, Q.; Lee, F.C. High performance coupled-inductor DC-DC converters. Applied Power Electronics Conference and Exposition, 2003. APEC '03. Eighteenth Annual IEEE, 2003, Vol. 1, pp. 109–113 vol.1.
9. Tseng, K.; Liang, T. Novel high-efficiency step-up converter. *Electric Power Applications, IEE Proceedings -* **2004**, *151*, 182–190.
10. Liang, T.; Tseng, K. Analysis of integrated boost-flyback step-up converter. *Electric Power Applications, IEE Proceedings -* **2005**, *152*, 217–225.
11. Xu, D.; Cai, Y.; Chen, Z.; Zhong, S. A novel two winding coupled-inductor step-up voltage gain boost-flyback converter. *2014 International Power Electronics and Application Conference and Exposition* **2014**, pp. 1–5.
12. Zhang, J.; Wu, H.; Xing, Y.; Sun, K.; Ma, X. A variable frequency soft switching boost-flyback converter for high step-up applications. 2011 IEEE Energy Conversion Congress and Exposition, 2011, pp. 3968–3973.
13. Ding, X.; Yu, D.; Song, Y.; Xue, B. Integrated switched coupled-inductor boost-flyback converter. 2017 IEEE Energy Conversion Congress and Exposition (ECCE), 2017, pp. 211–216.
14. Lai, C.M.; Yang, M.J. A High-Gain Three-Port Power Converter with Fuel Cell, Battery Sources and Stacked Output for Hybrid Electric Vehicles and DC-Microgrids. *Energies* **2016**, *9*.
15. Tseng, K.C.; Lin, J.T.; Cheng, C.A. An Integrated Derived Boost-Flyback Converter for fuel cell hybrid electric vehicles. 2013 1st International Future Energy Electronics Conference (IFEEC), 2013, pp. 283–287.
16. Park, J.H.; Kim, K.T. Multi-output differential power processing system using boost-flyback converter for voltage balancing. 2017 International Conference on Recent Advances in Signal Processing, Telecommunications Computing (SigTelCom), 2017, pp. 139–142.
17. Chen, S.M.; Wang, C.Y.; Liang, T.J. A novel sinusoidal boost-flyback CCM/DCM DC-DC converter. 2014 IEEE Applied Power Electronics Conference and Exposition - APEC 2014, 2014, pp. 3512–3516.
18. Lee, S.W.; Do, H.L. A Single-Switch AC-DC LED Driver Based on a Boost-Flyback PFC Converter With Lossless Snubber. *IEEE Transactions on Power Electronics* **2017**, *32*, 1375–1384.
19. Divya, K.M.; Paracka l, R. High power factor integrated buck-boost flyback converter driving multiple outputs. 2015 Online International Conference on Green Engineering and Technologies (IC-GET), 2015, pp. 1–5.
20. V. Acary, O.B.; Brogliato, B. *Nonsmooth Modeling and Simulation for Switched Circuits*; Springer, 2011.
21. Banerjee, S.; Verghese, G. *Nonlinear Phenomena in Power Electronics: Bifurcations, Chaos, Control, and Applications*; Wiley-IEEE Press, 2001.
22. Di Bernardo, M.; Budd, C.; Champneys, A.; Kowalczyk, P. *Piecewise-smooth Dynamical Systems, Theory and Applications*; Springer, 2008.
23. Carrero Candelas, N.A. Modelado, simulación y control de un convertidor boost acoplado magnéticamente. PhD thesis, Universidad Politécnica de Catalunya, 2014.
24. Munoz, J.G.; Gallo, G.; Osorio, G.; Angulo, F. Performance Analysis of a Peak-Current Mode Control with Compensation Ramp for a Boost-Flyback Power Converter. *Journal of Control Science and Engineering* **2016**.
25. Muñoz, J.G.; Gallo, G.; Angulo, F.; Osorio, G. Coexistence of solutions in a boost-flyback converter with current mode control. 2017 IEEE 8th Latin American Symposium on Circuits Systems (LASCAS), 2017, pp. 1–4.
26. Erickson, R.W.; Maksimovic, D. *Fundamentals of Power Electronics*; Springer, 2001.
27. Jiuming, Z.; Shulin, L. Design of slope compensation circuit in peak-current controlled mode converters. Electric Information and Control Engineering (ICEICE), 2011 International Conference on, 2011, pp. 1310–1313.
28. Grote, T.; Schafmeister, F.; Figge, H.; Frohleke, N.; Ide, P.; Bocker, J. Adaptive digital slope compensation for peak current mode control. Energy Conversion Congress and Exposition, 2009. ECCE 2009. IEEE, 2009, pp. 3523–3529.
29. Chen, Y.; Tse, C.K.; Wong, S.C.; Qiu, S.S. Interaction of fast-scale and slow-scale bifurcations in current-mode controlled DC/DC converters. *International Journal of Bifurcation and Chaos* **2007**, *17*, 1609–1622.

 doi:10.20944/preprints201809.0554.v1

Peer-reviewed version available at *Energies* **2018**, *11*, 3000; doi:10.3390/en11113000

30. Chen, Y.; Tse, C.K.; Qiu, S.S.; Lindenmuller, L.; Schwarz, W. Coexisting Fast-Scale and Slow-Scale Instability in Current-Mode Controlled DC/DC Converters: Analysis, Simulation and Experimental Results. *IEEE Transactions on Circuits and Systems I: Regular Papers* **2008**, *55*, 3335–3348.
31. Fang, C.C.; Redl, R. Subharmonic Instability Limits for the Peak-Current-Controlled Buck Converter With Closed Voltage Feedback Loop. *IEEE Transactions on Power Electronics* **2015**, *30*, 1085–1092.
32. Fang, C.C.; Redl, R. Subharmonic Instability Limits for the Peak-Current-Controlled Boost, Buck-Boost, Flyback, and SEPIC Converters With Closed Voltage Feedback Loop. *IEEE Transactions on Power Electronics* **2017**, *32*, 4048–4055.
33. El Aroudi, A. A New Approach for Accurate Prediction of Subharmonic Oscillation in Switching Regulators Part I: Mathematical Derivations. *IEEE Transactions on Power Electronics* **2017**, *32*, 5651–5665.
34. El Aroudi, A. A New Approach for Accurate Prediction of Subharmonic Oscillation in Switching Regulators Part II: Case Studies. *IEEE Transactions on Power Electronics* **2017**, *32*, 5835–5849.
35. Leine, R.I.; Nijmeijer, H. *Dynamics and Bifurcations of Non-Smooth Mechanical Systems*; Springer, 2004.
36. Dixon, L. Coupled Inductor Design. *Texas Instrument Incorporated* **2001**.